Indian Geotech J (October 2019) 49(5):531–542
https://doi.org/10.1007/s40098-019-00356-8

ORIGINAL PAPER

Insights into Effects of Seepage on Failure of Breakwater Mound: Experimental and Numerical Investigations

Mohammed Russedul Islam[1] · Kimitoshi Hayano[2] · Md. Aftabur Rahman[3]

Received: 19 October 2018 / Accepted: 25 February 2019 / Published online: 12 March 2019

Abstract Identifying the collapse mechanism of a breakwater mound caused by overtopping and seepage during extreme natural disasters is an essential element of a hazard mitigation policy. This research study conducts a set of experiments to quantify the effects of seepage and overtopping on the scouring of a breakwater. A scaled model of the Kamaishi breakwater in Japan, which was significantly damaged by the 2011 Great East Japan earthquake, is chosen for the tests. The experimental study reveals the significant influence of the hydraulic gradient of a breakwater on accelerating the depth of scouring. Then, a series of numerical simulations using smoothed particle hydrodynamics are carried out to justify the experimental outcomes and extract buried information which is normally not possible to be obtained from the experiments. Also, two countermeasures verified by the experimental and numerical models reveal significant reductions in the depth and width of scouring in a breakwater mound.

✉ Mohammed Russedul Islam
russed@ce.mist.ac.bd

Kimitoshi Hayano
hayano@ynu.ac.jp

Md. Aftabur Rahman
maftabur@cuet.ac.bd

[1] Department of Civil Engineering, Military Institute of Science and Technology, Mirpur, Dhaka 1216, Bangladesh

[2] Institute of Urban Innovation, Yokohama National University, 79-5 Tokiwadai, Hodogaya-ku, Yokohama 240-8501, Japan

[3] Department of Civil Engineering, Chittagong University of Engineering and Technology, Chittagong 4349, Bangladesh

Keywords Breakwater mound · Model test · Seepage · SPH · Two-phase flow · Tsunami scour

Introduction

Breakwaters, which constructed along the coastline, are a critically important structure to protect harbors from external damages. Impact and overtopping of waves are two major factors responsible for the damage of breakwaters. Mostly, overtopping of ocean waves during earthquake-induced tsunami is the primary cause of breakwater failure. Since the application of breakwaters, many instances of their failures have been reported in technical writings [1–6]. The most devastating event was recorded after the 2011 Great East Japan earthquake when the deepest breakwater called Kamaishi failed.

Seepage and scouring are the technical causes of the failures. Waves overtopped, and substantial variation of hydraulic head initiated seepage through the mound during the tsunami. Consequently, scouring occurred on the landside section and the bearing capacity of the mound decreased considerably [2, 7]. Research studies using physical and numerical methods have been conducted to gain insights into the failure mechanism of a breakwater mound [1, 3, 5, 7–10]. Also, experimental and numerical analyses of dyke failures owing to erosion caused by the impacts of waves and seepage flows have been carried out to determine their parametric sensitivities and failure patterns [11]. Mostly numerical analysis considers a grid-based approach; however, recently, some numerical simulations considering large deformation of geo-materials are conducted to observe the failure mechanism of dikes implicitly. For example, a new algorithm has been developed recently to describe the bank failure mechanism

implicitly and validated with experiments [12]. Also, other research studies comparing both experimental and numerical evaluations of embankment failures are available in the literature [11, 13, 14]. However, a numerical scheme on a Lagrangian platform may provide a better understanding of slope failures. Although a few discrete numerical tools have been used in geo-mechanics [15–17] with a background mesh, a truly Lagrangian approach has not been described. In contrast, a numerical method called smoothed particle hydrodynamics (SPH) [18] in a truly Lagrangian environment has recently become more attractive for engineering analyses and been applied in diverse fields of geotechnical engineering problems, specifically to analyze the geo-mechanics of large deformations [19–24]. The modeling of saturated soils considering both water and solid particles has also been conducted by researchers [25–27], while the failures of embankment slopes subject to seepage have been studied [28, 29] to evaluate different critical parameters.

SPH was initially developed to solve astrophysical problems [18], and, with further improvements in its features [30–33], its application has been extended to diverse fields of engineering, including hydrodynamics [34–38], viscous flows [39, 40], open-channel flows [41, 42], impact analyses [43] and sediment transport models, with a SPH scheme for geo-disaster and coastal engineering problems being recently implemented. Based on the diverse applications of SPH in large deformation problems, this research develops an updated SPH formulation that considers both soil and water particles in the numerical scheme described in the following subsections.

This research work considered a breakwater under different conditions. The effects of scouring and seepage on its failure were observed quantitatively from experimental investigations, and then, numerical simulations using a SPH scheme were performed to verify the model and extract buried information that could not be obtained from experiments. Moreover, different plausible countermeasures that could be used in practical problems were experimentally evaluated and justified by the numerical results.

Experimental Setups

As, of the different types of breakwaters, caisson ones are typically used in areas with rough waves, they are applied along many coastlines throughout the world. However, as constructing a real breakwater model in the laboratory is almost impossible, to check its compatibility with a real one, the law of similarity is a good option and used for the current research.

A 1/200th scaled model of the Kamaishi breakwater with a mound and caisson was prepared in a soil box, as shown in Fig. 1. In this experimental setup, the top and bottom widths of the mound were 22.5 cm and 88.5 cm, respectively, with the caisson, which was made of cement mortar and 12.5 cm high, 10.0 cm wide and 11.5 cm long mounted on the mound to absorb the wave energy and prevent overtopping. A tsunami overflow was produced for approximately 80 s using a Mariotte's tube tank [5], plastic pipeline and wooden channel, with the tube tank used to keep the flow rate constant during the overflow. Another Mariotte's tube tank and pipeline were set up to keep the water level on the seaside stable. The whirlpool's diameter, an indicator of scouring caused by overtopping, was kept constant for all the test cases, with the equation for estimating it as proposed by Noguchi et al. [44]:

$$R = g^{-\frac{1}{4}} q^{\frac{1}{2}} z_{\mathrm{f}}^{\frac{1}{4}} \tag{1}$$

where R is the whirlpool's diameter, q the flow rate and z_{f} the falling height. The flow rate and falling height were set to 8.5×10^{-3} ($\mathrm{m}^3/\mathrm{s/m}$) and 34.5 cm, respectively.

Four pressure gauge sensors were installed on the landside section to determine the breakwater's hydraulic gradient (Fig. 1b). The overtopping effect was applied by water falling from a certain height onto the landside section, while the same hydraulic head was maintained on both sides to discard the seepage.

Model Setups

A series of experimental setups were prepared to critically evaluate what happens to a breakwater during a tsunami or other disaster considering overtopping (Case A) and the combined action of overtopping and seepage (Cases B1, B2 and B3). As a difference between the hydraulic heads on the two sides plays a dominant role in seepage, differences of 5.0 cm, 6.0 cm and 7.0 cm were applied for the Case B types with both scouring and seepage considered. To efficiently resist the possible failure of a breakwater, widening its mound and sheet pile appears to be a good approach. Therefore, countermeasures using an increased mound size (Case C) and a combination of that and a larger sheet pile (Case D) were experimentally run to check the effectiveness of the individual models. For Case C, an extra 1.0-cm layer of soil was placed on the existing mound to widen it and raise its height, and then, a sheet pile was installed on the landside section (Case D). A total of six models were prepared, as summarized in Table 1.

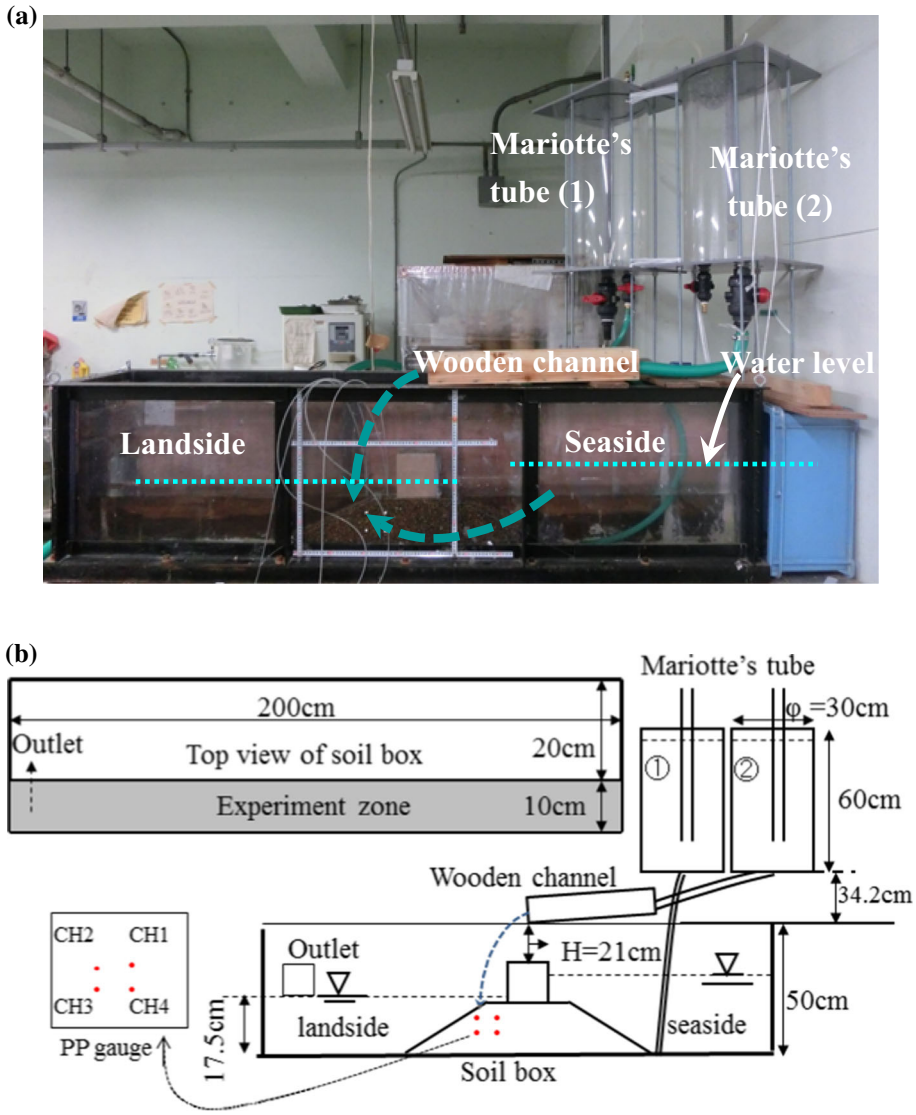

Fig. 1 **a** Photograph and **b** schematic diagram of model test arrangement

Table 1 Experimental conditions

Identification	Head difference (h) (cm)	Countermeasures	Description
Case A	0.0	None	Only overtopping
Case B_1	5.0	None	Overtopping and seepage
Case B_2	6.0	None	Overtopping and seepage
Case B_3	7.0	None	Overtopping and seepage
Case C	5.0	Widening and raising of embankment	Overtopping and seepage
Case D	5.0	Widening and raising of embankment + sheet pile	Overtopping and seepage

Experimental Results and Discussion

Deformations and Scouring of Breakwater Mounds

Cross-sectional profiles of the breakwater mounds for different cases were evaluated at different times, with a typical time history for Case A plotted in Fig. 2. It was found that the maximum scouring depth of the final profile was smaller than those of the intermediate ones, a phenomenon that demonstrated that scouring and collapses coincided in the model mounds. Also, comparing the scouring profiles with the applied countermeasures (Cases C and D), elevations of the top edges at the landside section were significantly higher than that of Case A which implies that, as the transportation of scoured soils was quite difficult, those soils probably resettled.

Maximum Depths and Widths of Scouring

The scouring profiles were recorded frame-wise and used to determine the depth and width of scouring. Figure 3 depicts the time histories of the scouring depths for all cases, where the overtopping time defines the time recorded when the overtopping water started falling from the wooden channel. Evolutions of the scouring widths for different scenarios plotted in Fig. 4 show that both scouring width and the scouring depths had higher values with increasing differences between the heads. For this discussion, Cases B_2 and B_3 are ignored because, as the boiling phenomena were so intense that their caissons collapsed after some time, it was not possible to record their data. As, based on the fundamentals of soil mechanics, seepage will increase with increases in the difference between the heads on the two sides, comparing Cases A and B_1, seepage considerably enhanced the scouring of the breakwater mound. This was probably because the flow of water through the mound decreased its bearing capacity and was ultimately responsible for the early collapse of the

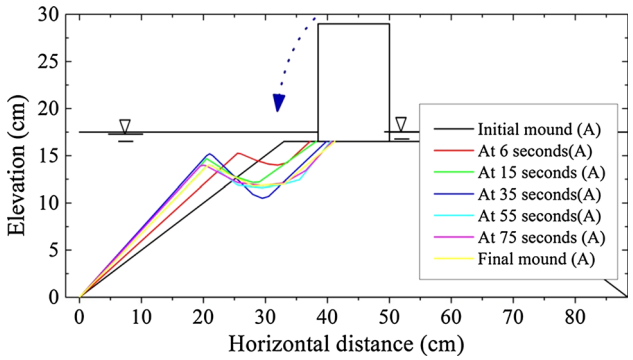

Fig. 2 Time history of surface profile of mound at landside section for Case A

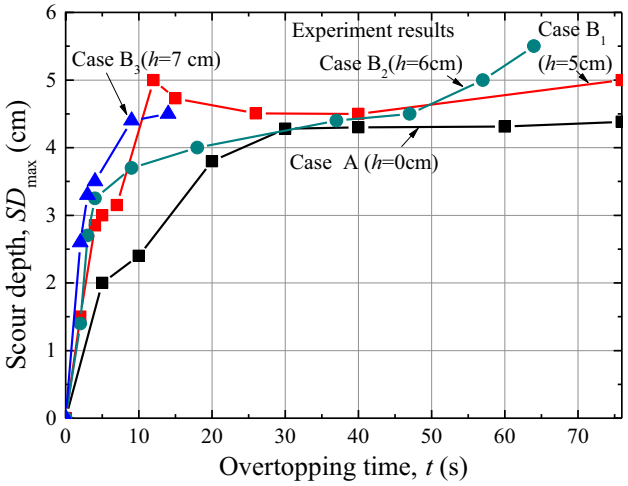

Fig. 3 Changes in scouring depths over time for various head differences obtained from experiments

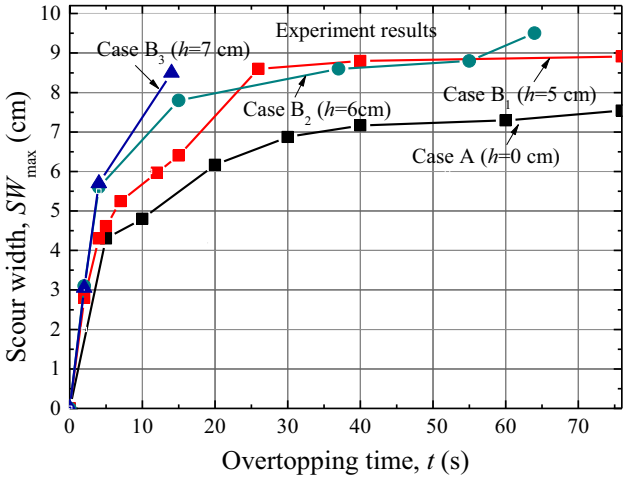

Fig. 4 Changes in scouring widths over time for various head differences obtained from experiments

breakwater. While evaluating the bearing capacity using experimental investigations is difficult, a numerical simulation can be an excellent option for extracting information that cannot be obtained from experiments. To address this crucial issue, the numerical simulations of breakwater mounds conducted are discussed in subsequent sections, with the relationships between the scouring depths and widths shown in Fig. 5. As they were dominant for Case B, this revealed the effect of seepage on the response of the breakwater mound while they decreased with applications of the countermeasures.

Hydraulic Gradients

Figure 6 shows the relationships between the horizontal and vertical hydraulic gradients (i_x and i_y, respectively) in

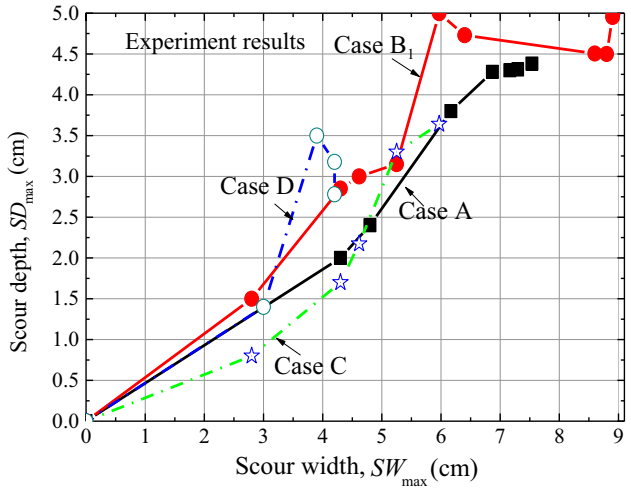

Fig. 5 Relationships between scouring depths and widths obtained from experiments

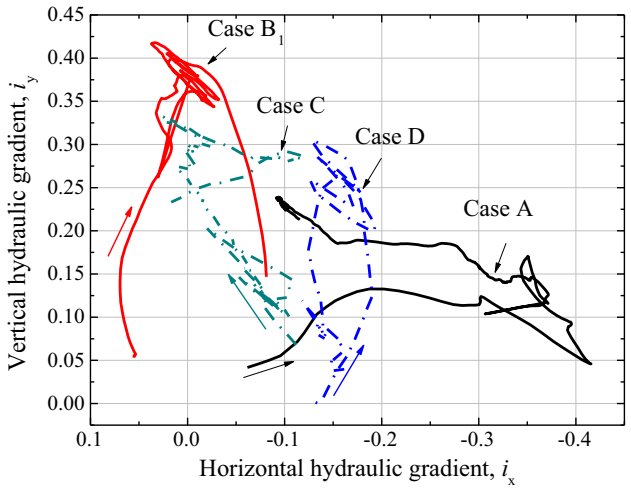

Fig. 6 Relationships between horizontal and vertical hydraulic gradients in mound obtained from experiments

the mound. The pore pressure gradients going down toward the landside and surface were taken as positives for i_x and i_y, respectively. Case B1 had a maximum ($(i_y)_{max}$) of 0.42 and minimum ($(i_y)_{min}$) of 0.05, whereas Case A had a $(i_y)_{max}$ of 0.24 and $(i_y)_{min}$ of 0.03. The differences between these hydraulic gradients might have been a result of their different scouring depths (Fig. 5). The $(i_y)_{max}$ of Cases C and D was 0.33 and 0.30, respectively, which was lower than that of Case B1 which might have contributed to the decreases in scouring depths in cases where countermeasures were taken. However, Case D had a maximum/greater vertical gradient than Case C which may have been due to some leakage of the seepage water between the sheet pile and soil box.

Numerical Simulations of Scouring

This numerical study attempted to simulate the deformation behavior of a breakwater mound due to scouring under similar conditions to those of the experiments. However, a/the traditional grid-based method may not be a suitable choice for modeling this large deformation problem as severe mesh distortions occur during a simulation which lead to inaccurate results and even a complete blowup of the system [45]. Recently, particle-based numerical tools have been used extensively by researchers conducting large deformation analyses. As, of many methods, SPH is one of the most promising because of its pure particle nature [46], it was used to numerically model breakwater mounds in this study.

Fundamentals of SPH

SPH is a particle method in which the computational domain is discretized into a finite number of integration points, each of which contains a definite domain known as a particle. The properties of each particle are adjusted using a smoothing kernel, with mass and momentum equations solved and integrated into each time step to update the positions of the particles. As there is no connectivity among the particles in the problem domain, SPH is a true particle method.

The fundamental formulation of SPH is based on the integral representations and particle approximations of field functions, with a field function $f(x_i)$ and its derivative $\nabla \cdot f(x_i)$, respectively:

$$f(x_i) = \sum_{j=1}^{N} \frac{m_j}{\rho_j} f(x_j) W(x_i - x_j, h) \tag{2}$$

$$\langle \nabla \cdot f(x_i) \rangle = \sum_{j=1}^{N} \frac{m_j}{\rho_j} f(x_j) . \nabla_i W_{ij} \tag{3}$$

where i is a particle, j its neighbor, N the total number of neighboring particles, h the smoothing length that defines the domain of influence of the smoothing kernel, $W(x_i - x_j, h)$ or W_{ij} the kernel or smoothing function and $\nabla_i W_{ij}$ the derivative of the smoothing kernel, $\nabla_i W_{ij} = \frac{x_i - x_j}{r_{ij}} \frac{\partial W_{ij}}{\partial r_{ij}}$, where r_{ij} is the distance between particles i and j.

Although several kernel functions are available in technical writings, a cubic spline has been used in most SPH applications [46] because it is similar to the Gaussian function which is considered a good selection as it is very stable and accurate. While a cubic spline function has the advantages of a Gaussian one plus compact support, this research work formulates it as:

$$W(q,h)=\alpha_{\mathrm{d}}\begin{cases}1.5-q^2+0.5q^3 & 0\le q<1\\ \dfrac{(2-q)^3}{6} & 1\le q<2\\ 0 & q\ge 2\end{cases} \tag{4}$$

where $q=\left|x_i-x_j\right|/h$ and $\alpha_{\mathrm{d}}=\frac{1}{h},\frac{15}{7\pi h^2},\frac{3}{2\pi h^3}$, respectively, in one, two and three dimensions.

Governing Equations

The Navier–Stokes equations, which are the governing ones employed in a SPH formulation, are:

$$\frac{\mathrm{d}\rho_i}{\mathrm{d}t}=\sum_{j=1}^{N}m_j\left(v_i^{\beta}-v_j^{\beta}\right)\nabla_i W_{ij} \tag{5}$$

$$\frac{\mathrm{d}v_i^{\beta}}{\mathrm{d}t}=\sum_{j=1}^{N}m_j\frac{\sigma_i^{\alpha\beta}+\sigma_j^{\alpha\beta}}{\rho_i\rho_j}\nabla_i W_{ij} \tag{6}$$

where $\sigma_i^{\alpha\beta}$ is the stress tensor which can be written as:

$$\sigma_i^{\alpha\beta}=-p\delta^{\alpha\beta}+\tau_i^{\alpha\beta} \tag{7}$$

where p is the pressure term, $\delta^{\alpha\beta}$ Kronecker's delta and $\tau_i^{\alpha\beta}$ the viscous stress determined by the appropriate constitutive law.

As an entire system can sometimes implode owing to the oscillations and penetrations of particles, to dissipate excess energy, it has been suggested that an artificial viscosity term be included in the momentum equation [47], with the equations of the artificial viscosity parameters:

$$\Pi_{ij}=\begin{cases}\dfrac{-\alpha_{\Pi}c_{ij}\phi_{ij}+\beta_{\Pi}\phi_{ij}^2}{\rho_{ij}} & v_{ij}x_{ij}<0\\ 0 & v_{ij}x_{ij}>0\end{cases} \tag{8}$$

$$\phi_{ij}=\frac{h_{ij}v_{ij}x_{ij}}{\left|x_{ij}\right|^2+\left(0.1h_{ij}\right)^2} \tag{9}$$

$$h_{ij}=\frac{h_i+h_j}{2} \tag{10}$$

$$\rho_{ij}=\frac{\rho_i+\rho_j}{2} \tag{11}$$

$$c_{ij}=\frac{c_i+c_j}{2} \tag{12}$$

Constitutive Relationship: Two-Phase SPH Model

Developing an appropriate constitutive law is the most challenging task of a numerical simulation, with the accuracy of its results being dependent mainly on how the materials are modeled. Neither the widely used constitutive law of soils nor a constitutive model of water would be satisfactory for the current breakwater analysis. As the breakwater mounds consisted of saturated soils represented by both soil and water particles, to accurately predict their responses, realistically modeling both the soils and water was a prerequisite. Therefore, a two-phase model that accounted for soil behavior in the current SPH scheme was developed. In it, both solid and water particles were represented by their material properties, with the seepage force acting as the interaction between them. A schematic diagram of this soil–water relationship is shown in Fig. 7.

A solid element in saturated soils was modeled using the elastic–perfectly plastic Drucker–Prager (D–P) failure criteria. The D–P model has proven its practical application in many soil mechanics problems [6, 21, 48–51], and its yield criterion is:

$$f(I_1,J_2)=\sqrt{J_2}+I_1\alpha_{\emptyset}-k_c=0 \tag{13}$$

where I_1 and J_2 are the first and second invariants of the stress tensor, respectively, defined by:

$$I_1=\sigma'^{xx}+\sigma'^{yy}+\sigma'^{zz} \tag{14}$$

$$J_2=\frac{1}{2}s'^{\alpha\beta}s'^{\alpha\beta} \tag{15}$$

where σ'^{xx}, σ'^{yy} and σ'^{zz} are the effective stress components in the directions of the x-, y- and z-axes, respectively, $s'^{\alpha\beta}$ the deviatoric effective shear stress tensor and $\alpha_{\emptyset}$ and k_{c} the two D–P constants in the plane strain condition which are related to the soil's cohesion (c) and frictional angle ($\emptyset$), respectively, as:

$$\alpha_{\emptyset}=\frac{\tan\emptyset}{\sqrt{9+12\tan^2\emptyset}} \tag{16}$$

$$k_{\mathrm{c}}=\frac{3c}{\sqrt{9+12\tan^2\emptyset}} \tag{17}$$

In this study, the non-associated plastic flow rule was adopted, with the plastic potential function (g_{p}) given by:

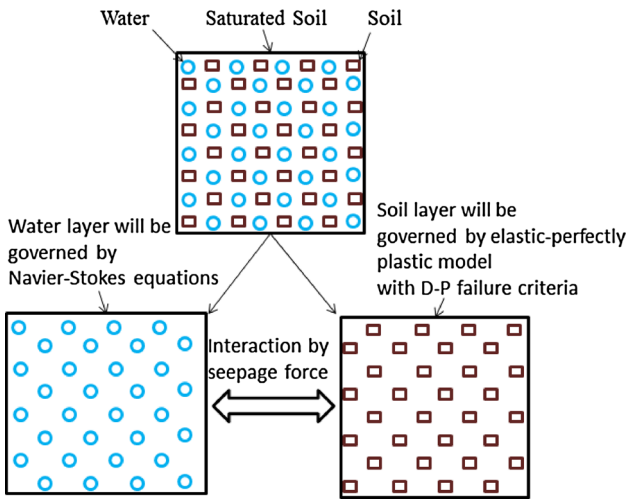

Fig. 7 Conceptual diagram of two-phase model of soil and water

$$g_{\mathrm{p}} = \alpha_{\psi} I_1 + \sqrt{J_2} - \text{constant} \tag{18}$$

$$\alpha_{\psi} = \frac{\tan\psi}{\sqrt{9 + 12\tan^2\psi}} \tag{19}$$

where α_{ψ} is the dilatancy factor and ψ the dilation angle.

The form of the stress–strain relationship considering the Jaumann stress rate for the D–P model is:

$$\frac{\mathrm{d}\sigma'^{\alpha\beta}}{\mathrm{d}t} = \sigma'^{\alpha\gamma}\dot{\omega}^{\beta\gamma} + \sigma'^{\gamma\beta}\dot{\omega}^{\alpha\gamma} + 2G\dot{e}^{\alpha\beta} + K\dot{e}^{\gamma\gamma}\delta^{\alpha\beta} - \dot{\lambda}\left[3K\alpha_{\psi}\delta^{\alpha\beta} + \frac{G}{\sqrt{J_2}}s'^{\alpha\beta}\right] \tag{20}$$

where

$$\dot{\omega}^{\alpha\beta} = \frac{1}{2}\left(\frac{\partial v^{\alpha}}{\partial x^{\beta}} - \frac{\partial v^{\beta}}{\partial x^{\alpha}}\right) \tag{21}$$

$$\dot{e}^{\alpha\beta} = \dot{\varepsilon}^{\alpha\beta} - \frac{1}{3}\dot{\varepsilon}^{\alpha\beta}\delta^{\alpha\beta} \tag{22}$$

$$s'^{\alpha\beta} = \sigma'^{\alpha\beta} - 1/3\sigma'^{\gamma\gamma}\delta^{\alpha\beta} \tag{23}$$

$$K = \frac{E}{3(1-2\nu)} \tag{24}$$

$$G = \frac{E}{2(1+\nu)} \tag{25}$$

$$\dot{\varepsilon}^{\alpha\beta} = \frac{1}{2}\left(\frac{\partial v^{\alpha}}{\partial x^{\beta}} + \frac{\partial v^{\beta}}{\partial x^{\alpha}}\right) \tag{26}$$

$$\dot{\lambda} = \frac{3\alpha_{\emptyset}K\dot{\varepsilon}^{\gamma\gamma} + \frac{G}{\sqrt{J_2}}s^{\alpha\beta}\dot{\varepsilon}^{\alpha\beta}}{9\alpha_{\emptyset}K\alpha_{\psi} + G} \tag{27}$$

where $\dot{\omega}^{\alpha\beta}$ is the spin rate tensor, $\dot{e}^{\alpha\beta}$ the deviatoric shear strain rate tensor, $\dot{\varepsilon}^{\alpha\beta}$ the strain rate tensor, K the bulk modulus of elasticity, G the shear modulus of elasticity, E the Young's modulus of elasticity, ν the Poisson's ratio and $\dot{\lambda}$ the rate of change in the plastic multiplier.

To identify the interaction between the soil and water, the seepage force exerted on the soil particles was obtained by [52]:

$$f = \gamma_{\mathrm{w}} n \frac{(v_{\mathrm{water}} - v_{\mathrm{soil}})}{k} \tag{28}$$

where γ_{w} is the unit weight of the water, n the porosity and k the permeability coefficient of the soil.

In this two-phase model, the momentum equation for the soil was:

$$\frac{Dv_i^{\alpha}}{Dt} = \sum_{j=1}^{N} m_j \frac{\sigma'_i + \sigma'_j}{\rho_i\rho_j}\frac{\partial W_{ij}}{\partial x_i^{\beta}} - \prod_{ij}\delta^{\alpha\beta} + \sum_{a=1}^{N} m_a \frac{\gamma_w n\frac{(v_a - v_i)}{k}}{\rho_i\rho_a}W_{ia} - \sum_{j=1}^{N}\frac{m_j}{\rho_i\rho_j}(p_{wj} - p_{wi})\frac{\partial W_{ij}}{\partial x_i^{\alpha}} + g_i^{\alpha} \tag{29}$$

where i is a particle representing the soil, j its soil neighbor, a its water neighbor, σ' the effective stress obtained from the soil's constitutive relationship and p_{wi} and p_{wj} the pore water pressure on the respective soil particles.

On the other hand, the water particles were modeled as a Newtonian fluid with the total stress composed of two parts: the pressure and viscous stress tensor. In the traditional SPH formulation, the pressure is estimated using the equation of state:

$$p = B\left[\left(\frac{\rho}{\rho_0}\right)^{\gamma} - 1\right] \tag{30}$$

And the viscous stress tensor for the Newtonian fluid model can be represented as:

$$\tau = \mu\dot{\gamma} \tag{31}$$

where μ is the dynamic viscosity and $\dot{\gamma}$ the shear strain rate.

The momentum equation for the water was:

$$\frac{Dv_a^{\alpha}}{Dt} = -\sum_{b=1}^{N} m_b \frac{p_a + p_b}{\rho_a\rho_b}\frac{\partial W_{ab}}{\partial x_a^{\beta}} + \sum_{b=1}^{N} m_b \frac{\mu_a\varepsilon_a^{\alpha\beta} + \mu_b\varepsilon_b^{\alpha\beta}}{\rho_a\rho_b}\frac{\partial W_{ab}}{\partial x_a^{\beta}} - \prod_{ab}\delta^{\alpha\beta} - \sum_{i=1}^{N} m_i \frac{\gamma_w n\frac{(v_a - v_i)}{k}}{\rho_i\rho_a}W_{ia} + g_a^{\alpha} \tag{32}$$

where a is a particle representing the water, b its water neighbor, i its soil neighbor, p its isotropic pressure, μ its dynamic viscosity, Π its artificial viscosity, $\delta^{\alpha\beta}$ the Dirac delta function and g is the body force which, in this case, is the gravitational force as it is the only one.

Boundary Treatment

The major drawback of a SPH simulation is the error occurring near the boundary of the domain due to the deficiency of particles. Therefore, a repulsive force transferred from the boundary particles to real ones to prevent the penetration of the latter beyond the problem domain is used in many technical papers on SPH simulations. However, previous repulsive force methods did not provide satisfactory results, with a complete implosion of the particles happening in some cases. Therefore, to obtain a rational solution, Morris and Monaghan [31] developed a new type of boundary particle known as a non-slip one. In their method, three layers of boundary particles were placed outside the problem domain and these particles contributed to real particles in the velocity and stress gradients. This type of boundary particle also had stress components, as implemented by Bui et al. [49] whereby, if a boundary particle (j) was within the support domain of a real particle (i), the stress would be assigned according to:

$$\sigma_j^{\alpha\beta} = \sigma_i^{\alpha\beta} \tag{33}$$

where α and β denote the Cartesian components x, y and z, with the Einstein convention applied to the repeated indices.

Modeling Scouring Using SPH

Using the same model, five cases identical to those in the experimental setup were prepared in the SPH environment as described in Table 2. For Case B types, considering the computational cost, only two hydraulic heads were chosen while the height of the mound was 10 cm instead of 16.5 cm because the maximum scour depth in the experiment was less than 6.0 cm. In Case D, the sheet pile was represented as an elastic material with a high elastic modulus revealing almost rigid obstacles while the mound was considered a frictional material with a typical frictional angle (φ) of 38°, Poisson's ratio (v) of 0.35 and bulk modulus of elasticity (K) of 16.7 MPa representing the mound in experimental conditions. The flow rate maintained from the inlet zone for all cases was set to 0.015(m^3/s/m) and the falling height (z_f) to 0.135 m. This combination of q and z_f made the whirlpool's diameter (R) in each simulation approximately 0.04 m, similar to that in the experiment. The initial stress on the mound was provided by a gravity loading method with a damping force applied and then the overtopping water was allowed to fall into the saturated mound for about 1.70 s for Case A. However, for all the other cases, based on the head difference between the sea- and landsides, a seepage flow was allowed to occur for approximately 2.0 s before the start of overtopping. Although this followed the process of the experiment, the time was adjusted in accordance with the computational capacity. The parameters for the simulations of all cases are given in Table 3.

Table 3 Simulation parameters for Case A

Initial particle spacing (m), Δd	0.005
Smoothing length (m), *hsml*	0.006
Duration of time step (s), Δt	10^{-5}
Density of soils (kg/m^3)	2008
Density of water (kg/m^3)	1000
Theoretical coefficient of permeability (cm/s), k	0.10
Porosity, n	0.50
Frictional angle of soil (degree), ϕ (c = 0)	38
Artificial viscosity parameters α, β for soil	0.1, 0.1
Artificial viscosity parameters α, β for water	0.1, 0
XSPH coefficient, ε, for water	0.01
Boundary type at rigid base	Non-slip
Boundary type at vertical wall	Symmetrical

Results of Numerical Simulations

Scouring Profiles

The scouring profiles for the different cases were found to be similar to that of the experimental results. Although scouring was observed in all cases, its depth and width depended on the seepage condition and application of countermeasures. The grains of soil detached by the impacts of the overtopping water and seepage force were the dominant factors for scouring. Comparing the general trends of the experiments and simulations confirmed the adverse effects of a tsunami's overflow and seepage on a breakwater mound, with the numerical simulations enabling hidden information that could not be extracted during experiments to be found. To quantify their effects on the scouring mechanism, the seepage forces for two cases (A and B1) are plotted in Fig. 8. Their distributions indicated the extent of the seepage phenomena on the landside section while a failure plan, which might have been responsible for the ultimate failure of the mound, was also seen.

Table 2 Simulation conditions

Identification	Head difference (h) (cm)	Countermeasures	Description
Case A	0.0	None	Only overtopping
Case B_1	5.0	None	Overtopping and seepage
Case B_2	7.5	None	Overtopping and seepage
Case C	5.0	Widening and raising of embankment	Overtopping and seepage
Case D	5.0	Widening and raising of embankment + sheet pile	Overtopping and seepage

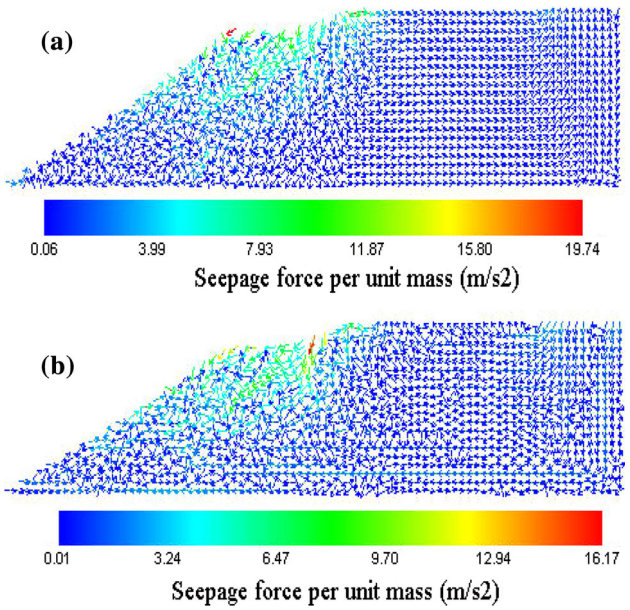

Fig. 8 Seepage forces at 0.5 s for **a** Case A and **b** Case B1

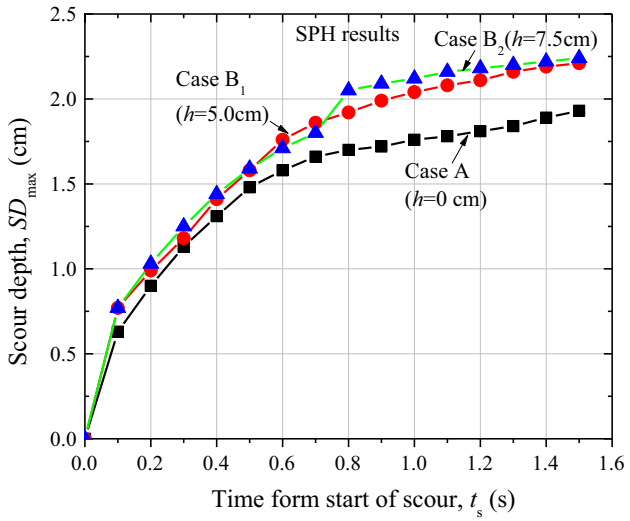

Fig. 9 Changes in scouring depths over time for various head differences obtained from SPH simulations

Maximum Depths and Widths of Scouring

The time histories of the scouring profiles recorded frame-wise and used to determine the maximum scouring widths and depths are plotted in Figs. 9 and 10, respectively. Both the width and depth responses were the same as those obtained from the experiments but their magnitudes were slightly less owing to the scaling effect of the numerical model. An interesting trend was observed in the relationships between the scouring depths and widths for Cases A, B1, C and D (Fig. 11). The depth and width for Case B_1 were approximately 0.30 cm and 0.40 cm higher than those

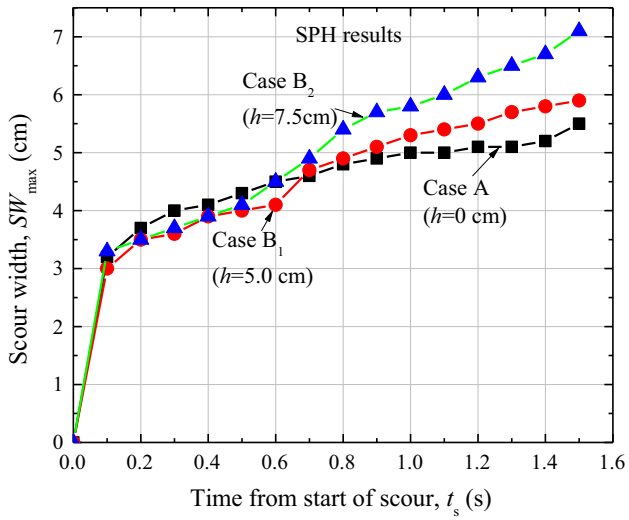

Fig. 10 Changes in scouring widths over time for various head differences obtained from SPH simulations

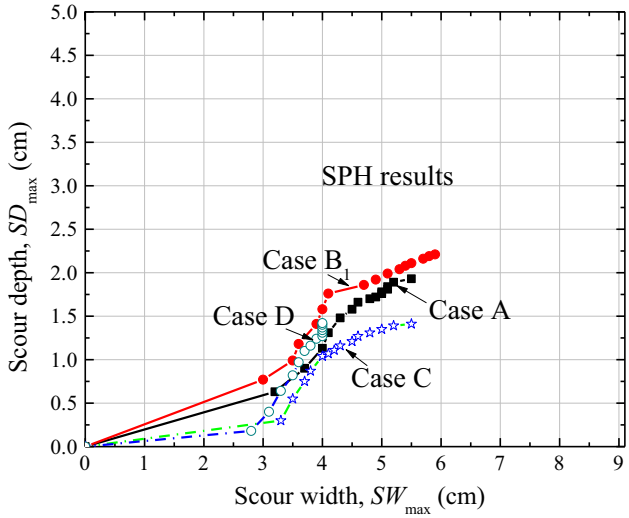

Fig. 11 Relationships between scouring depth and width obtained from SPH simulations

for Case A. Although this difference appeared to be small, it qualitatively proved the influence of the seepage force on scouring due to differences between the heads. The depths and widths for Cases C and D were lower than those for Case B_1 because countermeasures were installed for them. Also, it was noted that the relationships between the depths and widths of scouring followed similar trends in the simulations and experiments.

Bearing Capacity of Mound

Before the start of overtopping, a slip surface was formed for Case B_1, as shown in Fig. 12, but not for Case A which did not have a difference between heads. The maximum

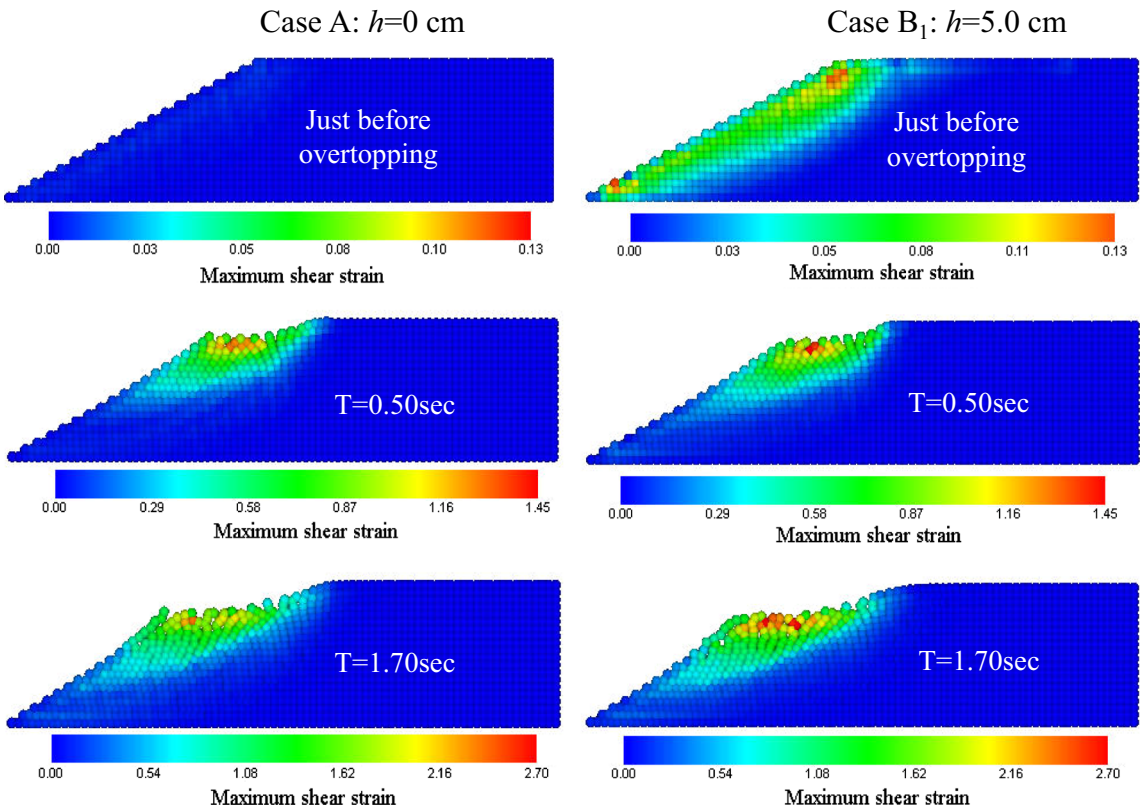

Fig. 12 Comparison of maximum shear strain distributions for Cases A and B_1 obtained from SPH simulations

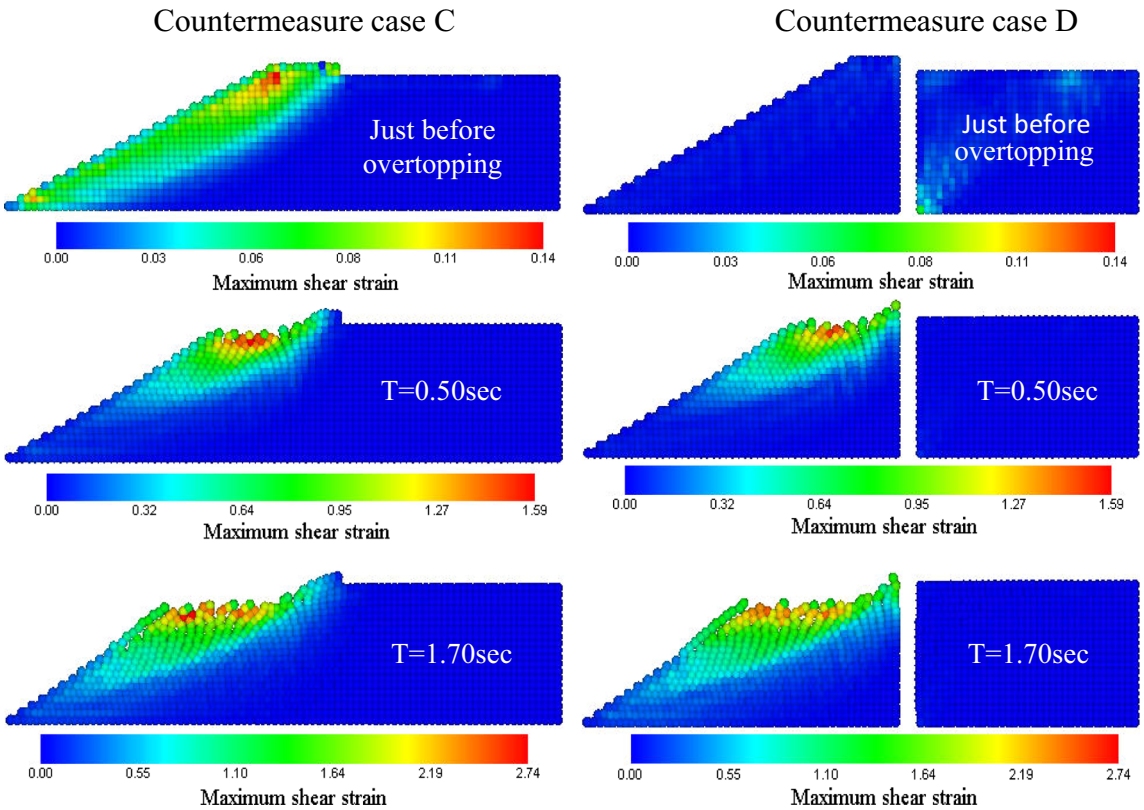

Fig. 13 Comparison of maximum shear strain distributions for Cases C and D obtained from SPH simulations

shear strain was found to increase significantly for both these cases after the start of overtopping, with that for Case B_1 showing higher values. This implicitly indicated that the bearing capacity of the mound was significantly reduced due to the existence of a difference between the heads on the seaside and landside. Similar trends of the maximum shear strain distributions for Cases C and D were found, as shown in Fig. 13, with the presence of the sheet pile in Case D stopping the seepage flowing from the seaside to landside. Given its reduced bearing capacity and the impact force caused by overtopping likely to lead to more scouring, the scouring depth and width for Case B_1 were higher than those for Case A.

Conclusions

A small-scale experimental investigation of a breakwater mound followed by a series of numerical simulations was conducted for this research study. The effects of seepage forces on the failure of a breakwater mound during extreme natural events were checked, with the model tests successfully exploring the scouring mechanism in the mound. The maximum scouring depth and width obtained from only overtopping were found to be less than those when overtopping was combined with seepage, with both increasing with higher seepage forces. Then, the results from numerical simulations carried out using a SPH scheme were found to be compatible with the experimental ones. Also, insights into a breakwater mound, such as the reduction in its bearing capacity, were provided by the numerical outcomes which implicitly described the effect of seepage forces. Two countermeasures which were tested both experimentally and numerically showed significant reductions in scouring. However, while this research is only a primary step in an investigation into the failure of a breakwater mound owing to tsunami overtopping, it can be extended to cover more complex and rational scenarios.

Acknowledgements The authors would like to thank Professor Kazuo Konagai and Associate Professor Mamoru Kikumoto at the Institute of Urban Innovation, Yokohama National University, for their valuable suggestions during this study.

References

1. Chaudhary B, Hazarika H (2018) Centrifuge modelling for stability evaluation of a breakwater foundation subjected to an earthquake and a tsunami. Ocean Eng 148:169–181. https://doi.org/10.1016/j.oceaneng.2017.11.005
2. Tanimoto K, Takahashi S (1994) Design and construction of caisson breakwaters—the Japanese experience. Coast Eng 22:57–77. https://doi.org/10.1016/0378-3839(94)90048-5
3. Kato F, Suwa Y, Watanabe K, Hatogai S (2012) Mechanisms of coastal dike failure induced by the Great East Japan Earthquake Tsunami. Coast Eng Proc 1:1–9. https://doi.org/10.9753/icce.v33.structures.40
4. Kazama M, Noda T (2012) Damage statistics (summary of the 2011 off the Pacific Coast of Tohoku earthquake damage). Soils Found 52:780–792. https://doi.org/10.1016/j.sandf.2012.11.003
5. Takahashi H, Sassa S, Morikawa Y et al (2014) Stability of caisson-type breakwater foundation under tsunami-induced seepage. Soils Found 54:789–805. https://doi.org/10.1016/j.sandf.2014.07.002
6. Dai Z, Huang Y, Cheng H, Xu Q (2014) 3D numerical modeling using smoothed particle hydrodynamics of flow-like landslide propagation triggered by the 2008 Wenchuan earthquake. Eng Geol 180:21–33. https://doi.org/10.1016/j.enggeo.2014.03.018
7. Zen K, Kasama K, Kasugai Y, Dong S (2013) Failure of rubble mound beneath caisson due to earthquake-induced tsunami. In: Proceedings of the ASME 2013 32nd international conference on ocean, offshore and arctic engineering, pp 1–8
8. Jianhong Y, Dongsheng J, Ren W, Changqi Z (2013) Numerical study of the stability of breakwater built on a sloped porous seabed under tsunami loading. Appl Math Model 37:9575–9590. https://doi.org/10.1016/j.apm.2013.05.006
9. Arikawa T, Sato M, Shimosako K et al (2012) Failure mechanism of Kamaishi breakwaters due to the Great East Japan earthquake tsunami. Coast Eng Proc 1:13. https://doi.org/10.9753/icce.v33.structures.16
10. Imase T, Maeda K, Miyake M et al (2012) Destabilization of a caisson-type breakwater by scouring and seepage failure of the seabed due to a tsunami. In: 6th International conference on scour erosion, pp 807–814
11. Di Cristo C, Evangelista S, Greco M et al (2018) Dam-break waves over an erodible embankment: experiments and simulations. J Hydraul Res 56:196–210. https://doi.org/10.1080/00221686.2017.1313322
12. Evangelista S, Greco M, Iervolino M et al (2015) A new algorithm for bank-failure mechanisms in 2D morphodynamic models with unstructured grids. Int J Sediment Res 30:382–391. https://doi.org/10.1016/j.ijsrc.2014.11.003
13. Evangelista S (2015) Experiments and numerical simulations of dike erosion due to a wave impact. Water (Switzerland) 7:5831–5848. https://doi.org/10.3390/w7105831
14. Aureli F, Dazzi S, Maranzoni A et al (2015) Experimental and numerical evaluation of the force due to the impact of a dam-break wave on a structure. Adv Water Resour 76:29–42. https://doi.org/10.1016/j.advwatres.2014.11.009
15. Nagata N, Hosoda T, Muramoto Y (2000) Numerical analysis of river channel processes with bank erosion. J Hydraul Eng 126:243–252
16. Stecca G, Measures R, Hicks DM (2017) A framework for the analysis of noncohesive bank erosion algorithms in morphodynamic modeling. Water Resour Res 53:6663–6686. https://doi.org/10.1002/2017WR020756
17. Martinelli M, Rohe A, Soga K (2017) Modeling dike failure using the material point method. Procedia Eng 175:341–348. https://doi.org/10.1016/j.proeng.2017.01.042
18. Lucy LB (1977) A numerical approach to the testing of the fission hypothesis. Astron J 82:1013–1024
19. Bui HH, Fukagawa R, Sako K, Ohno S (2008) Lagrangian meshfree particles method (SPH) for large deformation and failure flows of geomaterials using elastic–plastic soil constitutive model. Int J Numer Anal Methods Geomech 32:1537–1570. https://doi.org/10.1002/nag
20. Huang Y, Zhang W, Mao W, Jin C (2011) Flow analysis of liquefied soils based on smoothed particle hydrodynamics. Nat Hazards. https://doi.org/10.1007/s11069-011-9851-3

21. Chen W, Qiu T (2012) Numerical simulations for large deformation of granular materials using smoothed particle hydrodynamics method. Int J Geomech 12:127–135. https://doi.org/10.1061/(ASCE)GM.1943-5622.0000149
22. Zhang W, Maeda K (2015) SPH simulations for slope and levee failure under heavy rainfall considering the effect of air phase. In: Oka F, Murakami A, Uzuoka R, Kimoto S (eds) Computer methods and recent advances in geomechanics. Taylor & Francis Group, London, pp 1465–1470
23. Rahman MA, Konagai K (2017) A hands-on approach to estimate debris flow velocity for rational mitigation of debris hazard. Can Geotech J 55:941–955. https://doi.org/10.1139/cgj-2017-0211
24. Rahman MA, Konagai K (2017) Substantiation of debris flow velocity from super-elevation: a numerical approach. Landslides 14:633–647. https://doi.org/10.1007/s10346-016-0725-3
25. Grabe J, Stefanova B (2014) Numerical modeling of saturated soils, based on smoothed particle hydrodynamics (SPH): part 1: seepage analysis. Geotechnik 37:191–197. https://doi.org/10.1002/gete.201300024
26. Stefanova B, Seitz K, Bubel J, Grabe J (2012) Water–soil interaction simulation using smoothed particle hydrodynamics. In: 6th international conference on scour and erosion—ICSE-6: Paris, August 27–31, 2012, pp 695–704
27. Jian W, Liang D, Shao S et al (2015) SPH study of the evolution of water–water interfaces in dam break flows. Nat Hazards 78:531–553. https://doi.org/10.1007/s11069-015-1726-6
28. Zhang W, Maeda K, Saito H et al (2016) Numerical analysis on seepage failures of dike due to water level-up and rainfall using a water–soil-coupled smoothed particle hydrodynamics model. Acta Geotech 11:1401–1418. https://doi.org/10.1007/s11440-016-0488-y
29. Maeda K, Sakai H, Sakai M (2006) Development of seepage failure analysis method of ground with smoothed particle hydrodynamics. Struct Eng Earthq Eng 23:775–786
30. Monaghan JJ, Kocharyan A (1995) SPH simulation of multi-phase flow. Comput Phys Commun 87:225–235. https://doi.org/10.1016/0010-4655(94)00174-Z
31. Morris JP, Monaghan JJ (1997) A switch to reduce SPHnext viscosity. J Comput Phys 136:41–50
32. Monaghan JJ (1997) SPH and Riemann solvers. J Comput Phys 136:298–307. https://doi.org/10.1006/jcph.1997.5732
33. Monaghan JJ (2000) SPH without a tensile instability. J Comput Phys 159:290–311. https://doi.org/10.1006/jcph.2000.6439
34. Molteni D, Colagrossi A (2009) A simple procedure to improve the pressure evaluation in hydrodynamic context using the SPH. Comput Phys Commun 180:861–872. https://doi.org/10.1016/j.cpc.2008.12.004
35. Crespo AJC, Gómez-Gesteira M, Dalrymple RA (2008) Modeling dam break behavior over a wet bed by a SPH technique. J Waterw Port Coast Ocean Eng 134:313–320. https://doi.org/10.1061/(ASCE)0733-950X(2008)134:6(313)
36. Ran Q, Tong J, Shao S et al (2015) Advances in water resources incompressible SPH scour model for movable bed dam break flows. Adv Water Resour 82:39–50
37. Ferrari A, Dumbser M, Toro EF, Armanini A (2009) A new 3D parallel SPH scheme for free surface flows. Comput Fluids 38:1203–1217. https://doi.org/10.1016/j.compfluid.2008.11.012
38. Zheng X, Duan W (2010) Numerical simulation of dam breaking using smoothed particle hydrodynamics and viscosity behavior. J Mar Sci Appl. https://doi.org/10.1007/s11804-010-8037-9
39. Fang J, Owens RG, Tacher L (2006) A numerical study of the SPH method for simulating transient viscoelastic free surface flows. J Non-Newton Fluid 139:68–84. https://doi.org/10.1016/j.jnnfm.2006.07.004
40. Shao JR, Li HQ, Liu GR, Liu MB (2012) An improved SPH method for modeling liquid sloshing dynamics. Comput Struct 101:18–26. https://doi.org/10.1016/j.compstruc.2012.02.005
41. Dalrymple RA, Rogers BD (2006) Numerical modeling of water waves with the SPH method. Coast Eng 53:141–147. https://doi.org/10.1016/j.coastaleng.2005.10.004
42. Ferrari A (2010) Advances in water resources SPH simulation of free surface flow over a sharp-crested weir. Adv Water Resour 33:270–276. https://doi.org/10.1016/j.advwatres.2009.12.005
43. Gomez-Gesteira M, Dalrymple RA (2004) Using a three-dimensional smoothed particle hydrodynamics method for wave impact on a tall structure. J Waterw Port Coast Ocean Eng 130:63–69
44. Noguchi K, Sato S, Tanaka S (1997) Large-scale experiments on tsunami overtopping and bed scour around coastal revetment. Proc Coastal Eng JSCE 44:296–300 **(in Japanese)**
45. Ceccato F (2014) Study of large deformation geomechanical problems with the material point method. PhD Dissertation, Università degli Studi di Padova
46. Liu GR, Liu MB (2003) Smoothed particle hydrodynamics: a meshfree particle method, 1st edn. World Scientific Publishing Co. Pte. Ltd, Singapore
47. Monaghan JJ, Gingold RA (1983) Shock simulation by the particle method SPH. J Comput Phys 52:374–389. https://doi.org/10.1016/0021-9991(83)90036-0
48. Bui HH, Fukagawa R (2011) An improved SPH method for saturated soils and its application to investigate the mechanisms of embankment failure: case of hydrostatic pore-water pressure. Int Numer Anal Methods Geomech. https://doi.org/10.1002/nag
49. Bui HH, Sako K, Fukagawa R, Wells JC (2008) SPH-based numerical simulations for large deformation of geomaterial considering soil-structure interaction. In: 12th International conference of international association for computer methods and advances in geomechanics (IACMAG), pp 570–578
50. Bui HH, Fukagawa R, Sako K, Wells JC (2011) Slope stability analysis and discontinuous slope failure simulation by elasto-plastic smoothed particle hydrodynamics (SPH). Géotechnique 61:565–574. https://doi.org/10.1680/geot.9.P.046
51. Chen W, Qiu T (2014) Simulation of earthquake-induced slope deformation using SPH method. Int J Numer Anal Methods Geomech. https://doi.org/10.1002/nag
52. Bui HH, Sako K, Fukagawa R (2007) Numerical simulation of soil–water interaction using smoothed particle hydrodynamics (SPH) method. J Terramech 44:339–346. https://doi.org/10.1016/j.jterra.2007.10.003